



HAL
open science

Convective Instability Underneath Midlevel Clouds: Comparisons between Numerical Simulations and VHF Radar Observations

Atsushi Kudo, Hubert Luce, Hiroyuki Hashiguchi, Richard Wilson

► **To cite this version:**

Atsushi Kudo, Hubert Luce, Hiroyuki Hashiguchi, Richard Wilson. Convective Instability Underneath Midlevel Clouds: Comparisons between Numerical Simulations and VHF Radar Observations. *Journal of Applied Meteorology and Climatology*, 2015, 54 (11), pp.2217-2227. 10.1175/JAMC-D-15-0101.1 . insu-01198441

HAL Id: insu-01198441

<https://insu.hal.science/insu-01198441>

Submitted on 9 Nov 2020

HAL is a multi-disciplinary open access archive for the deposit and dissemination of scientific research documents, whether they are published or not. The documents may come from teaching and research institutions in France or abroad, or from public or private research centers.

L'archive ouverte pluridisciplinaire **HAL**, est destinée au dépôt et à la diffusion de documents scientifiques de niveau recherche, publiés ou non, émanant des établissements d'enseignement et de recherche français ou étrangers, des laboratoires publics ou privés.

Convective Instability Underneath Midlevel Clouds: Comparisons between Numerical Simulations and VHF Radar Observations

ATSUSHI KUDO

Meteorological Research Institute, Tsukuba, and Japan Meteorological Agency, Tokyo, Japan

HUBERT LUCE

Toulon University, La Garde, France

HIROYUKI HASHIGUCHI

Research Institute for Sustainable Humanosphere, Kyoto University, Uji, Japan

RICHARD WILSON

Sorbonne Universités, UPMC Université Paris 6, CNRS/INSU, and LATMOS-IPSL, Paris, France

(Manuscript received 6 April 2015, in final form 12 August 2015)

ABSTRACT

Deep turbulent layers can sometimes be observed on the underside of clouds that extend above upper-level frontal zones. In a recent study based on 3D numerical simulations with idealized initial conditions, it was found that midlevel cloud-base turbulence (MCT) can result from Rayleigh–Bénard-like convection as a result of cooling by sublimation of precipitating snow into dry and weakly stratified subcloud layers. In the present study, numerically simulated MCT was compared with a turbulent layer detected by the very high-frequency (VHF) middle- and upper-atmosphere (MU) radar during the passage of an upper-level front topped by clouds. The simulations were initialized with thermodynamic parameters derived from simultaneous radiosonde data. It was found that some important features of the simulated MCT (such as the scale of convection and vertical wind velocity perturbations) agreed quantitatively well with those reported in radar observations. Even if the possibility of other generation mechanisms cannot be ruled out, the good agreement strongly suggests that the MU radar actually detected MCT.

1. Introduction

Atmospheric turbulence can cause discomfort and even injuries to aircraft passengers and crew. Because turbulence has multiple sources, it is important to study all possible generation mechanisms for a better achievement of predictions.

Kelvin–Helmholtz (KH) instability is a well-known source of clear-air turbulence and is expected to occur in frontal zones since they coincide with regions of statically stable and strong vertical shear of horizontal winds (Browning et al. 1973; Shapiro 1980; Lilly 1986).

Convective clouds can cause turbulence as a result of strong vertical wind velocity fluctuations in the cloud region (MacCready 1964; MacPherson and Isaac 1977). Near-cloud turbulence occurs outside of strong convective systems through gravity waves and their breaking, enhancement of vertical shear, radiative effects, and a combination of these mechanisms (Lane and Sharman 2008; Trier et al. 2010; Lane et al. 2012; Kim et al. 2014). Inertia–gravity waves produced by highly unbalanced flows can be a source of turbulence through the local modification of the environmental Richardson number to be less than a critical value (Knox 1997; McCann 2001; Koch et al. 2005). Mountain waves can also generate turbulence as a result of wave breaking, rotor and lower turbulence zone formation, and the reduction of local stabilities (Scorer 1949; Durran 1986; Doyle et al. 2005; Cohn et al. 2011).

Corresponding author address: Atsushi Kudo, Numerical Prediction Division, Japan Meteorological Agency, Chiyoda, Tokyo 100-8122, Japan.
E-mail: kudo@met.kishou.go.jp

Luce et al. (2010) described another source of turbulence below a cirrus cloud base on the basis of the very high-frequency (VHF) middle- and upper-atmosphere (MU) radar and Rayleigh–Mie lidar observations. They suggested that sublimation cooling of ice crystals underneath the cloud base produces convective instability. Wilson et al. (2014) also reported the presence of turbulent layers underneath midlevel clouds by using the MU radar and radiosonde observations, but they did not discuss the origin of the observed turbulence. Parker and Johnson (2004) examined front-fed convective lines with leading stratiform precipitation (FFLS systems) by using idealized numerical simulations. They found that inflowing air was destabilized by lifting and by the vertical profile of evaporation and melting, which helped to maintain the simulated FFLS systems; however, they did not mention turbulence in the destabilized layers. Turbulence led by Rayleigh–Bénard-like convection below the base of clouds extending above upper-level fronts is called midlevel cloud-base turbulence (MCT) by Kudo (2013). He showed the morphology, evolution, and occurrence conditions of MCT from 3D numerical simulations with idealized initial conditions. In particular, it was found that convection rolls can extend well below the frontal zone, down to a few kilometers of altitude, especially when the dry subcloud layer is weakly stratified. These simulation results are consistent with occurrences of turbulence reported by pilot reports (PIREPs). However, quantitative evaluation of the MCT simulations could not be done.

The purpose of this study is to compare the characteristics of MCT quantitatively between the MU radar observations and high-resolution 3D numerical simulations initialized with thermodynamic parameters derived from simultaneous radiosonde data. The observation data were collected during a radar-balloon field campaign in September 2011. Section 2 briefly describes the observation data and the numerical model. Section 3a presents the main characteristics of the turbulent layer detected by the MU radar in light of temperature, humidity, and wind profiles of an upper-air sounding simultaneously observed at the radar site. Section 3b presents the results of the numerical simulations and compares them with the radar observations.

2. Observation data and numerical model

a. Observation data

The MU radar is a 46.5-MHz beam-steering Doppler pulsed radar located at Shigaraki MU Observatory (34.85°N, 136.10°E, Japan) (Fukao et al. 1990). The

radar is mainly sensitive to air refractive index irregularities in both clear and cloudy air conditions through various backscattering mechanisms. Partial reflection from horizontally stratified temperature and humidity gradient sheets can cause strong enhancements of echo power at vertical incidence (e.g., Luce et al. 1995). On the contrary, Bragg scatter from turbulence can produce a weak angular (azimuthal and zenithal) dependence of the radar echo power if the turbulent refractive index irregularities are statistically homogeneous in all directions at half the radar wavelength (e.g., Doviak and Zrnić 1984; Röttger and Larsen 1990). Therefore, a weak angular dependence of echo power can be an indicator of isotropic turbulence. In addition, the variance of Doppler spectral peaks can be a measure of the intensity of vertical wind velocity fluctuations due to turbulence after a careful correction of the measured variance from nonturbulent contributions [e.g., see Dehghan and Hocking (2011) for a recent review]. The turbulent kinetic energy per unit mass (TKE) assuming isotropy of the turbulent wind velocity fluctuations is given by $3/2w_{\text{rms}}^2 \simeq 3/2\sigma_{\text{turb}}^2$, where w_{rms} is the root-mean-square of the vertical wind velocity fluctuations and σ_{turb} is its estimate obtained from Doppler radar spectra [for details, see Wilson et al. (2014)].

During September 2011, the MU radar was continuously operated to collect vertical profiles of echo power, vertical and horizontal winds, and Doppler spectral width at a time resolution of ~ 12 s in the altitudinal range of 1.32–20.24 km with three beam directions (vertical and 10° off zenith toward the north and east). The range resolution was 150 m for winds and spectral width and a few tens of meters for echo power owing to the range imaging technique using frequency diversity [e.g., see Luce et al. (2006) for a detailed description of the technique]. Vertical profiles of pressure, temperature, humidity, and zonal and meridional wind velocities were collected simultaneously during the radar operation by RS92G Vaisala radiosondes.

b. Numerical model

The numerical model used for the present study was the Japan Meteorological Agency Nonhydrostatic Model (JMA-NHM), which is a fully compressive model for research and numerical weather prediction (Saito et al. 2007). The grid spacing of both the vertical and horizontal grids was set to 50 m so that aircraft-scale turbulence (horizontal scales between ~ 100 and ~ 2000 m) could be resolved directly. The horizontal domain was $5000 \text{ m} \times 5000 \text{ m}$ with a periodic boundary condition, and the vertical domain extended from 0 to 10 000 m above mean sea level. The precipitation process was an explicit three-ice bulk microphysics scheme

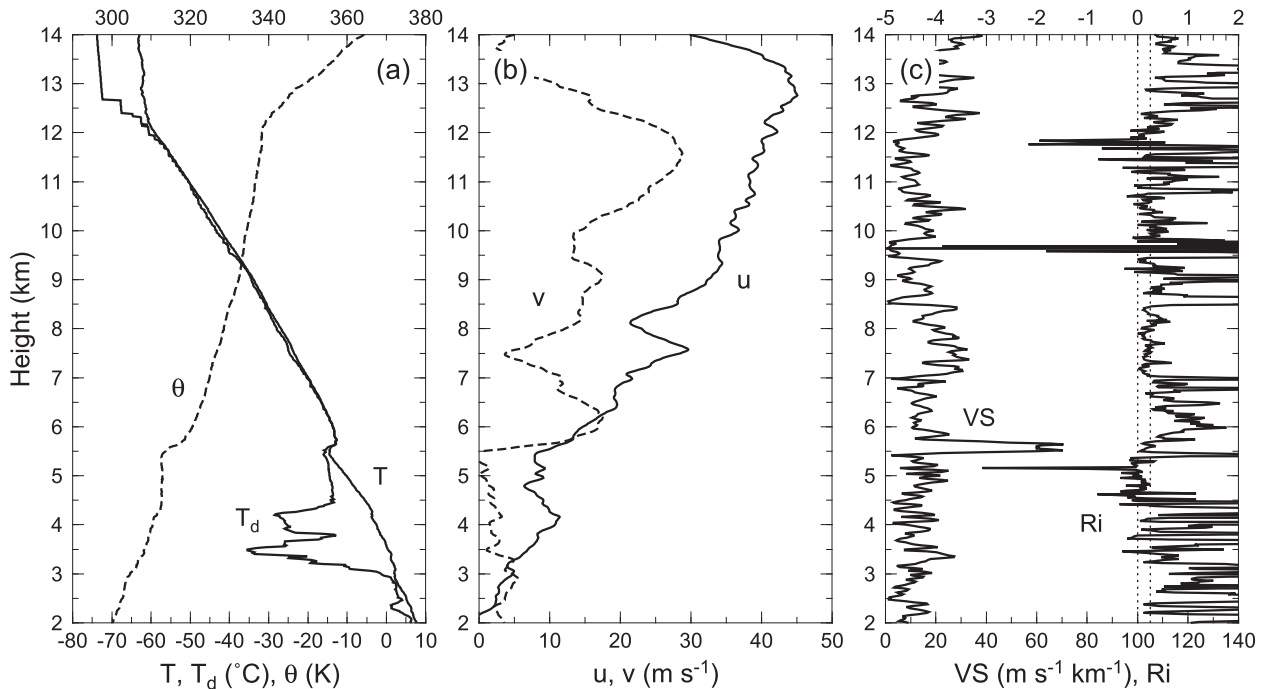


FIG. 1. Vertical profiles obtained from T52 of (a) temperature T , dewpoint temperature T_d , and potential temperature θ ; (b) meridional and zonal wind components u and v ; and (c) vertical shear of horizontal wind VS and the Richardson number Ri. The left and right vertical dotted lines in (c) indicate $Ri = 0.0$ and 0.25 , respectively. Each parameter is plotted at a constant vertical interval of 20 m. The VS and Ri were derived from the vertical difference of the wind and potential temperature at ± 20 m.

(Ikawa and Saito 1991) that considers six mixing ratios (water vapor, cloud liquid water, cloud ice, rain, snow, and graupel) and one number concentration (cloud ice). The Deardorff scheme (Deardorff 1980) was used for subgrid-scale turbulence, and the surface flux was not taken into account since it is likely irrelevant to midlevel phenomena. Since the model uses a periodic boundary condition, physical quantities (water vapor, momentum, heat, etc.) are not supplied from the boundary during the simulation period.

The initial conditions were derived from balloon observations. The original radiosonde data were first smoothed by spline interpolation to remove small-scale fluctuations and to improve the stability of the numerical simulation. Then, they were interpolated onto the vertical grids. Basically, the initial horizontal grids had uniform values, but random perturbations on a scale of 0.1% were added for the wind components and water vapor mixing ratio. Vertical wind velocity and hydrometeor (cloud liquid water, cloud ice, rain, snow, and graupel) mixing ratios were set to zero at the initial time.

Sensitivity experiments with vertical grid spacing of 25 m, horizontal grid spacing of 25 m, and a horizontal domain of $10000\text{ m} \times 10000\text{ m}$ showed that the results were almost the same as in the original experiment (not shown).

Those results suggest that the resolutions and domain set in the present study are enough to represent the MCT event.

3. Results

a. Balloon and radar observations

1) UPPER-AIR SOUNDING

During the night of 25–26 September 2011, five radiosondes were launched at a nearly constant 3-h time interval with the first launch at ~ 1700 local time (LT; hereinafter the five soundings are labeled as T49, T50, T51, T52, and T53 in order). Figure 1 shows the vertical profiles of temperature, dewpoint temperature, potential temperature, meridional and zonal wind velocities, vertical shear of horizontal wind (VS), and the Richardson number ($Ri = N^2/VS^2$, where N^2 is the squared Brunt–Väisälä frequency) in the 2.0–14.0-km height range obtained from T52 launched at 0238 LT. A remarkable increase in temperature with strong wind shear (due to the differential advection of two different air masses) associated with an upper frontal zone was observed at ~ 5.5 km. At the altitude of the front, Ri was around the critical value of 0.25. The air was saturated (therefore cloudy) above the front up to the altitude of

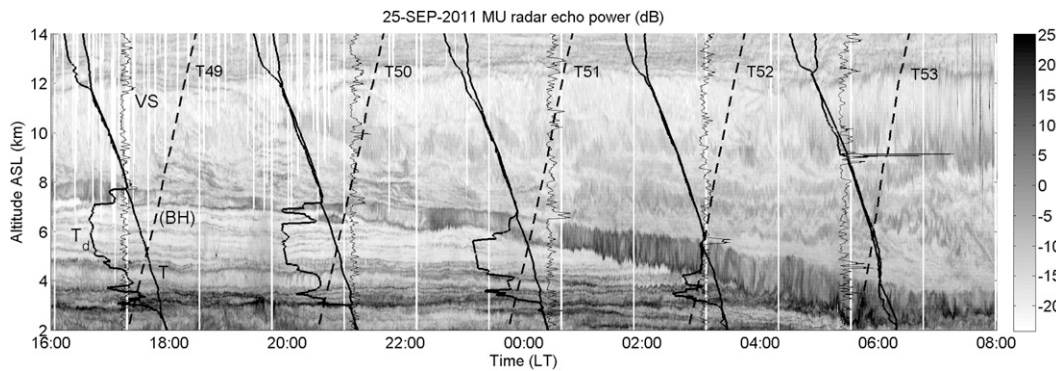


FIG. 2. Time–height cross section of radar echo power measured by the MU radar at vertical incidence in the height range 2.0–14.0 km from 1600 LT 25 Sep to 0800 LT 26 Sep 2011. Vertical profiles of T , T_d , and VS measured by the radiosondes launched at 1712, 2024, 2337, 0238, and 0529 LT (labeled T49–T53 in order) are superimposed for easy reference (without scales). The dashed lines indicate the height of balloons (BH) vs time. The radar was stopped for 2 min every 71 min for technical reasons. Missing data (due to radar stops and airplane interferences) are left blank.

~12.0 km and subsaturated below the front. The cloud-base temperature was about -12.5°C . Beneath the front, down to ~4.5 km, the stability was almost neutral and it was even convectively unstable in the lower part resulting in a partially negative Richardson number. On the basis of a Thorpe analysis (Thorpe 1977) of the potential temperature profile, Wilson et al. (2014) showed the presence of a turbulent layer with a depth of 1071 m at the mean altitude of 4921 m. Below ~4.5 km, the large difference between temperature and dewpoint temperature indicates that the air was very dry. The four other soundings showed qualitatively the same features except that the subcloud layers were not convectively unstable but only nearly neutral.

2) RADAR

A time–height cross section of radar echo power at vertical incidence from 1600 LT 25 September 2011 to 0800 LT 26 September in the 2.0–14.0-km height range shows an echo layer steadily descending from ~8.0 km at 1600 LT down to ~3.2 km at 0800 LT (Fig. 2). After ~0100 LT, the echo power within the layer was significantly enhanced and the layer depth increased with time. Cross sections of the radar echo power were similar at the two oblique incidences within the same height range (not shown), suggesting that the radar backscattering was isotropic and thus the atmosphere was turbulent in the layer. The top of the layer coincided with the height of the upper-level front shown in Fig. 1, suggesting that the time evolution of the layer top corresponded to that of the upper-level front and the cloud base. The radar echo power pattern changed around 12.0 km during the period. This change coincided with the boundary between moist and dry regions shown by

the soundings, indicating that this feature was associated with the cloud-top height.

Figure 3a shows a close-up of Fig. 2 from 0100 to 0500 LT on 26 September 2011 in the 2.0–8.0-km height range. The subsequent panels show the corresponding time–height cross sections of vertical wind velocity, TKE (see section 2a), and horizontal wind speed and direction. The temperature, dewpoint temperature, and vertical shear profiles measured by T52 are superimposed for easy reference. The echo power pattern shows nearly vertical striations with irregular and curved edges (Fig. 3a). The radar likely outlined the boundary of cells or billows where the refractive index fluctuations are expected to be the largest (e.g., Ottersten 1969). The layer depth increased with time from ~700 m at 0100 LT to ~1500 m at 0500 LT and was ~1200 m at 0300 LT (i.e., during the T52 balloon flight). The superimposed balloon profile confirms that turbulence occurred just below the frontal zone (i.e., beneath the temperature inversion, strong vertical shear, and the cloud base). The turbulent layer detected by the radar corresponded to the unstable or neutral layer where the dewpoint temperature was nearly constant. In addition, it was found to be within the range of the turbulent layer detected by a Thorpe processing of the radiosonde observations (Wilson et al. 2014). Interestingly, there was no apparent signature of the frontal zone itself in the radar echoes while it is recognized that a vertically pointed VHF radar can be used to observe the structure of frontal zones because of its sensitivity to stable layers (e.g., Larsen and Röttger 1985). A temporal alternation of positive and negative vertical wind velocities within the turbulent layer (Fig. 3b) is consistent with the presence of cells or billows. Up- and downdrafts were up to $\pm 2.3 \text{ m s}^{-1}$ and

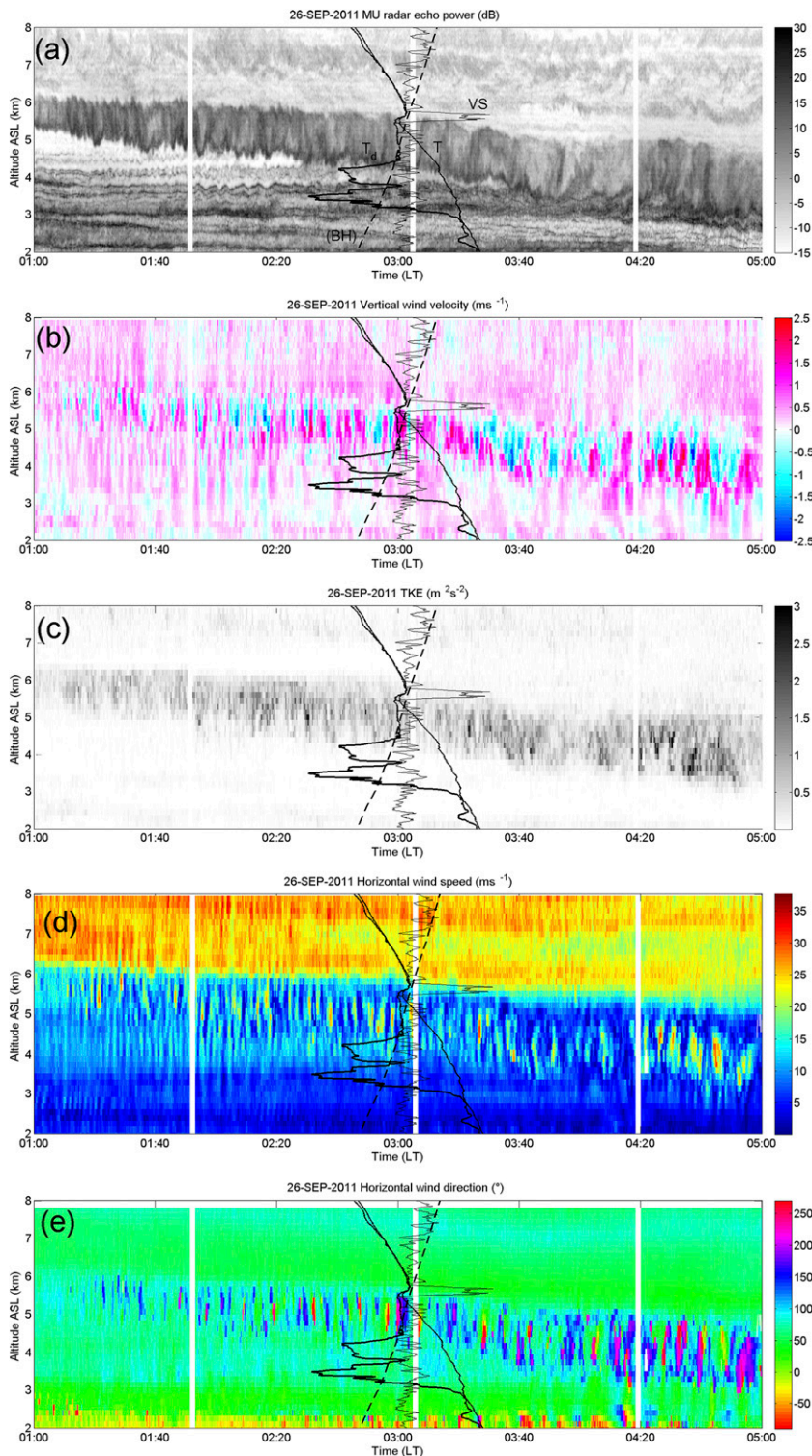


FIG. 3. Time–height cross sections of parameters measured by the MU radar from 0100 to 0500 LT 26 Sep 2011 in the height range 2.0–8.0 km: (a) radar echo power, (b) vertical wind velocity, (c) TKE, (d) horizontal wind speed, and (e) horizontal wind direction. As in Fig. 2, the T , T_d , and VS profiles measured by the balloon launched at 0238 LT (T52) are superimposed for easy reference. The dashed lines indicate BH vs time.

TKE was $0.63\text{--}0.85\text{ m}^2\text{ s}^{-2}$ around the balloon flight and they were maximum after 0420 LT. Above the front (i.e., in the cloudy region), the radar echoes were less intense, and the vertical wind velocity fluctuations and TKE were much weaker. The horizontal wind speed and direction plots (Figs. 3d,e) confirm a strong vertical shear of horizontal wind at the frontal zone as a result of wind speed and direction changes. The horizontal wind fluctuations within the turbulent layer can be the result of perturbations due to the cells or billows. However, these estimates are not quantitatively reliable because the method for retrieving horizontal wind components likely failed because of the nonuniformity of the wind field over the horizontal distance between the probed radar volumes. As a result, accurate estimates of the wind shear within the turbulent layer were impossible to obtain and reliable comparisons with estimates from balloon data could not be obtained. At the base of the turbulent layer, only a small stable gradient (temperature inversion) was detected and the balloon-derived wind shear was not enhanced. The radar-derived wind speed and direction plots also suggest the absence of significant wind shear at the layer base.

The characteristics of the radar echoes and vertical wind velocity fluctuations were not consistent with those produced by a KH instability (e.g., Fukao et al. 2011; Luce et al. 2012). Specifically,

- KH billows are usually identified by slanted “S shaped” structures in time–height cross sections of radar echo power; here, the structures were rather suggestive of large vortices generated by convection;
- even if the KH wave is an evanescent mode, KH billows produce vertical wind velocity perturbations far above and below the altitude of the billows; here, the largest vertical wind velocity fluctuations were limited to the nearly neutral or convectively unstable layer; and
- at the mean altitude of the turbulent layer, there was no amplitude minimum and no phase shift of the vertical wind velocity that would suggest a critical level of KH instability.

These arguments may be weakened if the observations were made after the KH billows broke and formed well-developed turbulence. However, the vertical redistribution of momentum produced by turbulent mixing would result in a shear layer splitting so that the shear would be minimal near the center of the layer and maximal at its edges (e.g., Woods 1968). Because neither balloon nor radar data revealed enhanced shear at the layer base and the time series of balloons (Fig. 2) shows that vertical shear was weak below cloud base during the whole period, this mechanism is unlikely. The

observations suggest that the initial shear was weak when the instability developed.

In summary, turbulence observed by the MU radar on 26 September 2011 below a frontal zone was very likely MCT. The temperature at the cloud base (-12.5°C) and the weak stratification and low humidity below the frontal zone observed by T52 (Fig. 1) are also consistent with conditions related to the occurrence of MCT according to the simulations by Kudo (2013).

b. Simulation results and comparisons with the radar observations

To compare the MU radar observations with numerical simulations quantitatively, we performed high-resolution 3D numerical simulations initialized with the parameters derived from the balloon data described in section 3a(1). Figure 4 presents a result of the simulation for T52, which shows horizontal sections of simulated parameters at a height z of 4900 m at $t = 65, 75,$ and 90 min after the initial time, and vertical sections along the averaged horizontal wind direction at $z = 4900\text{ m}$ and $t = 75\text{ min}$. At $t = 65$ and 75 min, ordered up- and downdrafts appeared at around $z = 4900\text{ m}$. They were aligned nearly perpendicular to the flow. The convection was located in the subcloud layer and extended about 1100 m at $t = 75\text{ min}$, in close agreement with the range and depth of the turbulent layer observed by the MU radar. The ordered convection began to decay after $t = 80\text{ min}$, and transitioned to relatively disordered convection at $t = 90\text{ min}$. Autocorrelations of the simulated vertical wind velocities along the east–west and the north–south axes at $z = 4900\text{ m}$ and $t = 75\text{ min}$ reached maxima at 1000 and 2300 m, respectively (not shown). It follows that the horizontal wavelength of the disturbances along the wind direction was 955 m and that the corresponding period was 114 s, because the averaged horizontal wind speed was 8.4 m s^{-1} and the wind direction was 7.3° counterclockwise from the east between 4350 and 5450 m.

Figures 5a and 5b show a time series of vertical wind velocities measured with the MU radar between 0153 and 0304 LT averaged in the 4.77–5.22-km height range and the corresponding frequency spectrum. Because the time series were sampled at intervals of $\sim 6.14\text{ s}$, the Nyquist frequency f_N was $\sim 0.08\text{ Hz}$. The frequency spectrum showed some peaks at frequencies smaller than $\sim 10^{-2}\text{ Hz}$. The time scale of the highest-frequency peak was $\sim 133\text{ s}$. Because an averaged radar-derived horizontal wind speed was about 9.3 m s^{-1} , the corresponding apparent horizontal wavelength for a period of 133 s was $\sim 1200\text{ m}$. Figures 5c and 5d show similar graphs at earlier time (between 2326 and 0037 LT) within the turbulent layer (between 6.42 and 6.87 km).

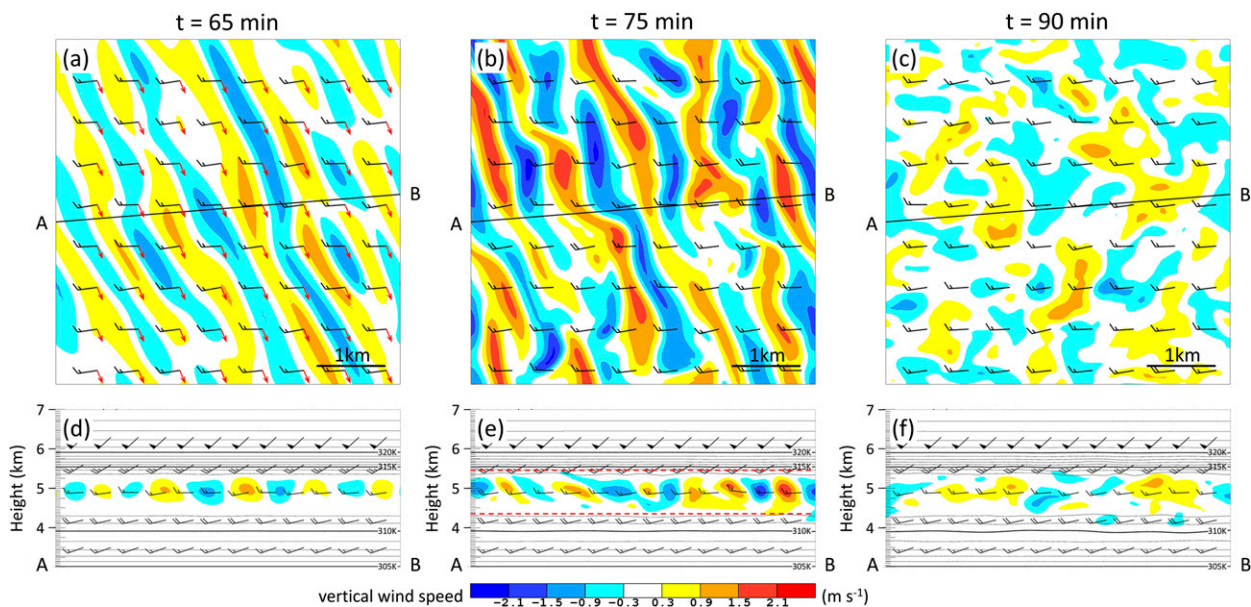


FIG. 4. Simulation results at $t = 65, 75,$ and 90 min for T52. (a)–(c) Horizontal sections showing vertical wind velocity (shading) and horizontal wind barbs at $z = 4900$ m. (d)–(f) Vertical sections showing vertical wind velocity (shading), horizontal wind barbs, and isentropes (solid lines) along the wind direction at $z = 4900$ m and $t = 75$ min [lines A–B in (a)–(c)]. The red arrows in (a) indicate vertical shear vectors between the top and bottom of the convectively unstable layer ($z = 5150$ and 4750 m) at the initial time ($t = 0$ min). The red dashed lines in (e) indicate the approximate vertical range of convection.

During that period, the time series and spectra showed weaker but nearly monochromatic fluctuations of period 100–110 s (around 1000 and 3000 s after 2326 LT in Fig. 5c), more consistent in appearance with the ordered

up- and downdrafts found from simulations before the disordered transition. These periods corresponded to horizontal wavelengths of ~ 1400 – 1500 m for a horizontal wind speed of ~ 14 m s^{-1} (not shown). These

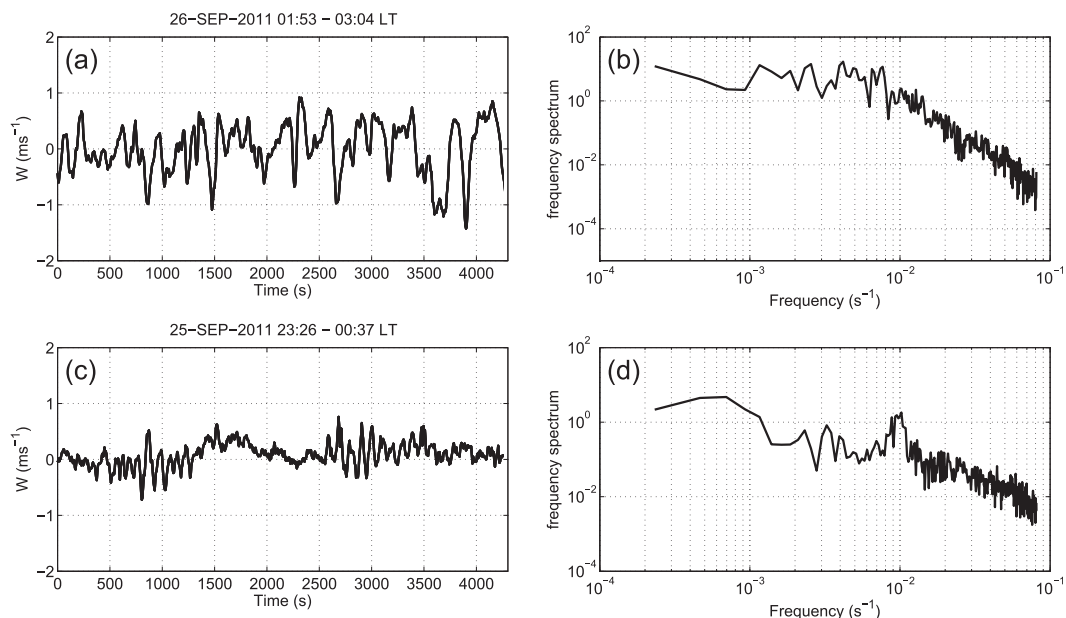


FIG. 5. (a) Time series of vertical wind velocities observed by the MU radar averaged between the altitudes of 4.77 and 5.22 km (within the turbulent layer) from 0153 to 0304 LT, and (b) the corresponding frequency spectrum. (c),(d) As in (a) and (b), but for vertical wind velocities averaged between the altitudes of 6.42 and 6.87 km from 2326 to 0037 LT.

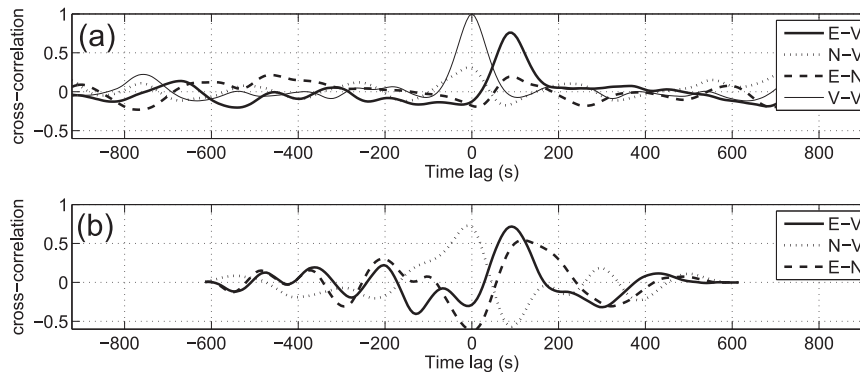


FIG. 6. (a) Cross-correlation functions between time series of detrended radial wind velocities (E = east, N = north, and V = vertical) observed by the MU radar averaged between the altitudes of 4.77 and 5.22 km (within the turbulent layer) from 0153 to 0304 LT (71 min). (b) As in (a), but for 10 min during the T52 balloon flight from 0234 LT.

radar observations indicate that vertical wind velocity disturbances similar to those produced at an early stage of the simulations can also be sporadically and locally observed in such real situations. In summary, considering the difficulty of obtaining reliable estimates from radar data under the horizontal inhomogeneity of the wind field, the periods and wavelengths observed by the MU radar agree quite well with those estimated from the simulation results.

In an attempt to quantify in more detail the degree of disorder of the convective cells observed by the MU radar in the turbulent layer, similarities between the time series of linearly detrended radial wind velocities obtained with the vertical, north, and east beams were estimated by calculating normalized cross-correlation functions. Figure 6 shows the results for the time series collected between 0153 and 0304 LT (71 min) and between 0234 and 0244 LT (10 min) averaged between 4.77- and 5.22-km altitude (within the turbulent layer). The cross-correlation functions between the east and vertical beams (i.e., along the east–west axis) showed a weak value (close to 0) at 0 lag but a significant peak (~ 0.7) at ~ 90 s in both cases. Because the horizontal wind was essentially eastward (zonal wind speed $\sim 9.3 \text{ m s}^{-1}$) at the mean altitude of the turbulent layer (5.2 km), the vertical and east beams should have detected the same structures but with a time delay corresponding to the horizontal distance between the probed radar volumes [here, $5200 \times \tan(10^\circ) \simeq 920 \text{ m}$] divided by the horizontal wind speed if the irregularities were frozenly advected by the wind field. A time delay of $920/0.3 = 99 \text{ s}$ was found, in close agreement with the value obtained from the cross-correlation analysis. The cross-correlation function between the north and vertical beams (i.e., along the north–south axis) showed a maximum at 0 lag but does not exceed ~ 0.3 for the sequence of 71 min. The cross correlation was sometimes higher for

shorter sequences (e.g., 0.7 for the selected sequence of 10 min). The cross-correlation function between the north and east beams had a weak maximum around 90 s, in accordance with the properties of the cross-correlation functions observed along the north–south and east–west axes. The cross correlations between the east and vertical beams suggest that the structures of convection were organized more or less into bands oriented approximately perpendicular to the wind direction (i.e., north–south). However, the lower cross correlations between the north and vertical beams suggest that the radar observed decayed bands or bands with superimposed random fine turbulent structures rather than pure 2D convection rolls. In fact, the simulation results first showed ordered convection followed by mainly disordered convection: the MU radar might have observed a later breaking stage of the convection.

Figure 7 shows vertical profiles of physical quantities obtained from the numerical simulations at $t = 0, 65, 75,$ and 90 min for T52. The vertical profiles of snow mixing ratio (Fig. 7d) showed snow generation above the stable layer, that is, in the cloudy region, and sublimation below the cloud base. Other hydrometeors (i.e., cloud liquid water, cloud ice, rain, and graupel) were not generated or were close to zero around the stable layer during the simulation. Sublimation of snow cooled the subcloud layer, which gradually expanded the convectively unstable layer so that its depth reached 550 m at $t = 65$ min (see Fig. 7a, potential temperature). This instability caused convection below the cloud base, and the vertical wind velocity and TKE attained maximum values of $\pm 2.4 \text{ m s}^{-1}$ and $0.76 \text{ m}^2 \text{ s}^{-2}$, respectively, at $t = 75$ min (Figs. 7e,f). These values agree very well with the corresponding values obtained from the radar observations of $\pm 2.3 \text{ m s}^{-1}$ and $0.63\text{--}0.85 \text{ m}^2 \text{ s}^{-2}$, respectively. After $t = 75$ min, convective mixing proceeded, the

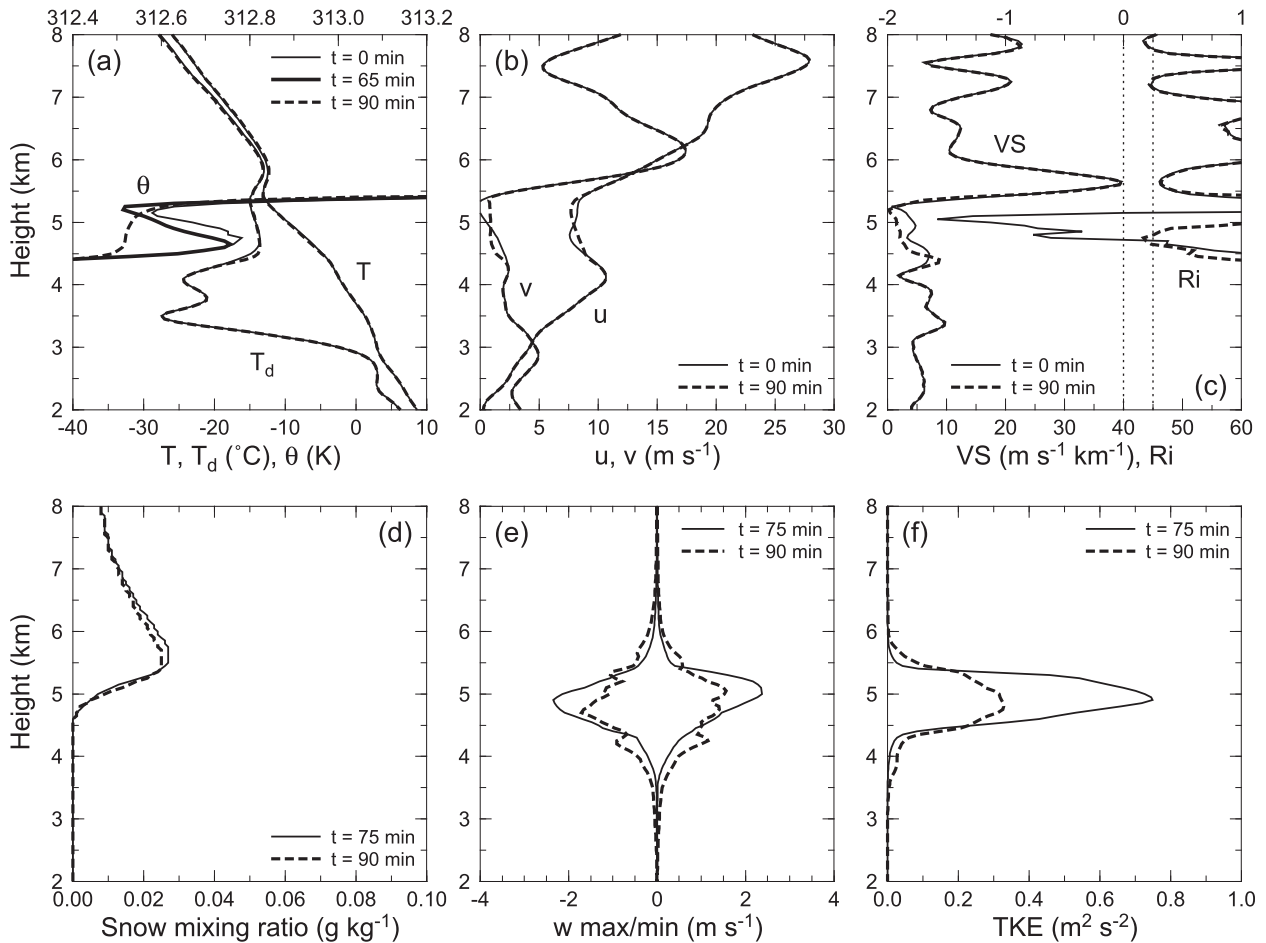


FIG. 7. Vertical profiles of physical quantities at $t = 0$ (initial conditions), 65, 75, and 90 min obtained from the simulations for T52. (a) Temperature T , dewpoint temperature T_d , and potential temperature θ ; (b) meridional and zonal wind velocities u and v ; (c) vertical shear of horizontal wind VS and the Richardson number Ri , where the left and right dotted lines indicate $Ri = 0.0$ and 0.25 , respectively; (d) snow mixing ratio; (e) maximum and minimum vertical wind velocities; and (f) TKE. Values in (a),(b), and (d) were the horizontal averages; those in (c) were calculated from horizontally averaged vertical profiles; those in (e) were the maximum and minimum in the horizontal plane; and those in (f) were based on wind speed fluctuations in the horizontal plane. The initial conditions were derived from T52 balloon observations. The observed parameters were smoothed to remove small-scale fluctuations and to improve the stability of the numerical calculations.

convective instability was removed, and a nearly neutral layer was generated in the subcloud region (Fig. 7a). At $t = 90$ min, vertical wind velocities and TKE became weaker (Figs. 7e,f), and the Richardson number became positive below the stable layer (Fig. 7c). During the simulation period, wind, temperature, and dewpoint temperature changed little, and vertical shear remained weak in the subcloud layer. In spite of the strong vertical shear at the height of the stable layer ($z = 5600$ m), the vertical wind velocities and TKE produced by the simulation at that height were very small (Figs. 7e,f) because the Richardson number was not small enough to generate a KH instability. This result is also consistent with the radar data, since KH billows were not detected by the MU radar at the stable cloud base.

Results of simulations initialized by the other soundings (i.e., T49, T50, T51, and T53) were generally consistent with the MU radar observations. Simulations for T49 and T50 showed that convection did not appear below cloud base (not shown) because the cloud-base temperatures were too low (lower than -20°C) to generate a large enough amount of snow precipitation. The MU radar also did not observe an intense echo layer (i.e., turbulence) below cloud base around the balloon flight of T49 and T50 (Fig. 2). For T51 and T53, as with the results of T52, simulations showed that convectively unstable layers were generated due to the sublimation of snow and then up- and downdrafts appeared below cloud base (not shown). The radar observations also showed turbulence or convection

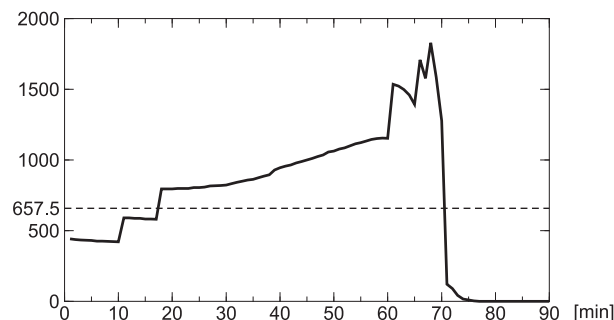


FIG. 8. Time series of the Rayleigh number in the subcloud layer calculated from the averaged vertical profiles in the simulation for T52. The dashed line indicates the critical Rayleigh number for the “both-ends free” condition. The steps at $t = 11, 18, 61, 66,$ and 68 min reflect discrete changes in the depth of the convectively unstable layer.

below cloud base around the balloon flights of T51 and T53 (Figs. 2 and 3b).

Ordered convection shown in Fig. 4 appeared under convectively unstable and weak vertical shear conditions, suggesting Rayleigh–Bénard-like convection. In fact, the direction of the initial vertical shear vectors in the convectively unstable layer ($z = 4750\text{--}5150$ m) slanted about 22.9° counterclockwise from the south (see red arrows in Fig. 4a), which well corresponded to the orientation of the wave front. Because convection rolls are usually aligned parallel to the vertical shear direction in the convectively unstable layer (Asai 1972), this characteristic is an additional argument for Rayleigh–Bénard convection. In addition, the Rayleigh number exceeded the critical value when the ordered convection appeared in the simulation. Figure 8 shows a time series of the Rayleigh number in the subcloud layer derived from the simulation for T52, defined as

$$Ra = \frac{g\Delta\theta d^3}{\bar{\theta}K_M K_\theta},$$

where g is gravity; $\Delta\theta$ and $\bar{\theta}$ are the difference of the potential temperature and its average in the convectively unstable layer, respectively; d is the depth; and K_M and K_θ are the eddy diffusivities for momentum and heat, respectively. Here, $K_M = K_\theta = 30\text{ m}^2\text{ s}^{-1}$ was used following Helfand and Kalnay (1983). In the present study, the critical Rayleigh number was 657.5 because the top and bottom boundaries of the unstable layer were free. The Rayleigh number exceeded the critical value at $t = 18$ min and attained a maximum value at $t = 68$ min, then rapidly dropped to zero at $t = 75$ min when the convection reached a maximum. Therefore, the evolution of the Rayleigh number also supports the conclusion that Rayleigh–Bénard convection was generated.

4. Summary and conclusions

During a field campaign in September 2011 at Shigaraki MU Observatory, the MU radar was operated continuously with high time and range resolutions and Vaisala radiosondes were launched simultaneously. The MU radar detected turbulence below a frontal zone (cloud base) where the atmosphere was convectively unstable and vertical shear was weak, consistent with MCT events described by Kudo (2013) on the basis of numerical simulations. To study the nature of the observed turbulence, we performed high-resolution 3D numerical simulations initialized with the balloon data and compared the results with those obtained from the MU radar observations. The simulations showed that ordered convection parallel to the vertical shear direction appeared after the Rayleigh number exceeded the critical value. The simulation results agreed well quantitatively with the MU radar observations. Both the observation and simulation results suggest independently that the convection below the cloud base was indeed very likely MCT (i.e., Rayleigh–Bénard convection). Parameters characterizing the convection were consistent between the simulation results and the radar observations, strongly suggesting that MCT was both observed by the MU radar and well reproduced by the numerical simulation. The present study appears to be consistent with the generation mechanism of MCT proposed by Kudo (2013). The possible consequences of these results on the studies presented by Wilson et al. (2014) for the present event will be considered in further works since Wilson et al. estimated turbulence parameters based on the hypothesis of shear-induced turbulence in stably stratified atmosphere.

Acknowledgments. We thank three anonymous reviewers for their constructive comments and suggestions that helped improve the manuscript. Part of this work was carried out at the Research Institute for Sustainable Humanosphere (RISH), Kyoto University, by one of the authors (HL), whose presence at RISH was supported first by the National Institute of Communications and Technology (NICT), later by a Japan Society for the Promotion of Science (JSPS) fellowship, and finally by an appointment as a visiting scientist. The MU radar belongs to and is operated by the RISH.

REFERENCES

- Asai, T., 1972: Thermal instability of a shear flow turning the direction with height. *J. Meteor. Soc. Japan*, **50**, 525–532.
- Browning, K. A., G. W. Bryant, J. R. Starr, and D. N. Axford, 1973: Air motion within Kelvin–Helmholtz billows determined from simultaneous Doppler radar and aircraft measurements.

- Quart. J. Roy. Meteor. Soc.*, **99**, 608–618, doi:10.1002/qj.49709942203.
- Cohn, S. A., V. Grubišić, and W. O. J. Brown, 2011: Wind profiler observations of mountain waves and rotors during T-REX. *J. Appl. Meteor. Climatol.*, **50**, 826–843, doi:10.1175/2010JAMC2611.1.
- Deardorff, J. W., 1980: Stratocumulus-capped mixed layers derived from a three-dimensional model. *Bound.-Layer Meteor.*, **18**, 495–527, doi:10.1007/BF00119502.
- Dehghan, A., and W. K. Hocking, 2011: Instrumental errors in spectral-width turbulence measurements by radars. *J. Atmos. Sol.-Terr. Phys.*, **73**, 1052–1068, doi:10.1016/j.jastp.2010.11.011.
- Doviak, R. J., and D. S. Zrnić, 1984: *Doppler Radar and Weather Observations*. Academic Press, 458 pp.
- Doyle, J. D., M. A. Shapiro, Q. Jiang, and D. L. Bartels, 2005: Large-amplitude mountain wave breaking over Greenland. *J. Atmos. Sci.*, **62**, 3106–3126, doi:10.1175/JAS3528.1.
- Durran, D. R., 1986: Mountain waves. *Mesoscale Meteorology and Forecasting*, P. S. Ray, Ed., Amer. Meteor. Soc., 472–492.
- Fukao, S., T. Sato, T. Tsuda, M. Yamamoto, and M. D. Yamanaka, 1990: MU radar: New capabilities and system calibrations. *Radio Sci.*, **25**, 477–485, doi:10.1029/RS025i004p00477.
- , H. Luce, T. Mega, and M. K. Yamamoto, 2011: Extensive studies of large-amplitude Kelvin–Helmholtz billows in the lower atmosphere with VHF middle and upper atmosphere radar. *Quart. J. Roy. Meteor. Soc.*, **137**, 1019–1041, doi:10.1002/qj.807.
- Helfand, H. M., and E. Kalnay, 1983: A model to determine open or closed cellular convection. *J. Atmos. Sci.*, **40**, 631–650, doi:10.1175/1520-0469(1983)040<0631:AMTDOO>2.0.CO;2.
- Ikawa, M., and K. Saito, 1991: Description of a non-hydrostatic model developed at the Forecast Research Department of the MRI. MRI Tech. Rep. 28, 238 pp.
- Kim, J.-H., H.-Y. Chun, R. D. Sharman, and S. B. Trier, 2014: The role of vertical shear on aviation turbulence within cirrus bands of a simulated western Pacific cyclone. *Mon. Wea. Rev.*, **142**, 2794–2813, doi:10.1175/MWR-D-14-00008.1.
- Knox, J. A., 1997: Possible mechanisms of clear-air turbulence in strongly anticyclonic flows. *Mon. Wea. Rev.*, **125**, 1251–1259, doi:10.1175/1520-0493(1997)125<1251:PMOCAT>2.0.CO;2.
- Koch, S. E., and Coauthors, 2005: Turbulence and gravity waves within an upper-level front. *J. Atmos. Sci.*, **62**, 3885–3908, doi:10.1175/JAS3574.1.
- Kudo, A., 2013: The generation of turbulence below midlevel cloud bases: The effect of cooling due to sublimation of snow. *J. Appl. Meteor. Climatol.*, **52**, 819–833, doi:10.1175/JAMC-D-12-0232.1.
- Lane, T. P., and R. D. Sharman, 2008: Some influences of background flow conditions on the generation of turbulence due to gravity wave breaking above deep convection. *J. Appl. Meteor. Climatol.*, **47**, 2777–2796, doi:10.1175/2008JAMC1787.1.
- , —, S. B. Trier, R. G. Fovell, and J. K. Williams, 2012: Recent advances in the understanding of near-cloud turbulence. *Bull. Amer. Meteor. Soc.*, **93**, 499–515, doi:10.1175/BAMS-D-11-00062.1.
- Larsen, M. F., and J. Röttger, 1985: Observations of frontal zone and tropopause structures with a VHF Doppler radar and radiosondes. *Radio Sci.*, **20**, 1223–1232, doi:10.1029/RS020i006p01223.
- Lilly, D. K., 1986: Instabilities. *Mesoscale Meteorology and Forecasting*, P. S. Ray, Ed., Amer. Meteor. Soc., 259–271.
- Luce, H., M. Crochet, F. Dalaudier, and C. Sidi, 1995: Interpretation of VHF ST radar vertical echoes from in situ temperature sheet observations. *Radio Sci.*, **30**, 1003–1025, doi:10.1029/95RS00713.
- , G. Hassenpflug, M. Yamamoto, and S. Fukao, 2006: High-resolution vertical imaging of the troposphere and lower stratosphere using the new MU radar system. *Ann. Geophys.*, **24**, 791–804, doi:10.5194/angeo-24-791-2006.
- , T. Nakamura, M. K. Yamamoto, M. Yamamoto, and S. Fukao, 2010: MU radar and lidar observations of clear-air turbulence underneath cirrus. *Mon. Wea. Rev.*, **138**, 438–452, doi:10.1175/2009MWR2927.1.
- , and Coauthors, 2012: Kelvin–Helmholtz billows generated at a cirrus cloud base within a tropopause fold/upper-level frontal system. *Geophys. Res. Lett.*, **39**, L04807, doi:10.1029/2011GL050120.
- MacCready, P. B., Jr., 1964: Standardization of gustiness values from aircraft. *J. Appl. Meteor.*, **3**, 439–449, doi:10.1175/1520-0450(1964)003<0439:SOGVFA>2.0.CO;2.
- MacPherson, J. I., and G. A. Isaac, 1977: Turbulent characteristics of some Canadian cumulus clouds. *J. Appl. Meteor.*, **16**, 81–90, doi:10.1175/1520-0450(1977)016<0081:TCOSCC>2.0.CO;2.
- McCann, D. W., 2001: Gravity waves, unbalanced flow, and aircraft clear air turbulence. *Natl. Wea. Dig.*, **25** (1–2), 3–14.
- Ottersten, H., 1969: Atmospheric structure and radar backscattering in clear air. *Radio Sci.*, **4**, 1179–1193, doi:10.1029/RS004i012p01179.
- Parker, M. D., and R. H. Johnson, 2004: Simulated convective lines with leading precipitation. Part II: Evolution and maintenance. *J. Atmos. Sci.*, **61**, 1656–1673, doi:10.1175/1520-0469(2004)061<1656:SCLWLP>2.0.CO;2.
- Röttger, J., and M. F. Larsen, 1990: UHF/VHF radar techniques for atmospheric research and wind profiler applications. *Radar in Meteorology*, D. Atlas, Ed., Amer. Meteor. Soc., 235–281.
- Saito, K., J. Ishida, K. Aranami, T. Hara, T. Segawa, M. Narita, and Y. Honda, 2007: Nonhydrostatic atmospheric models and operational development at JMA. *J. Meteor. Soc. Japan*, **85B**, 271–304, doi:10.2151/jmsj.85B.271.
- Scorer, R., 1949: Theory of waves in the lee of mountains. *Quart. J. Roy. Meteor. Soc.*, **75**, 41–56, doi:10.1002/qj.49707532308.
- Shapiro, M. A., 1980: Turbulent mixing within tropopause folds as a mechanism for the exchange of chemical constituents between the stratosphere and troposphere. *J. Atmos. Sci.*, **37**, 994–1004, doi:10.1175/1520-0469(1980)037<0994:TMWTFA>2.0.CO;2.
- Thorpe, S. A., 1977: Turbulence and mixing in a Scottish loch. *Phil. Trans. Roy. Soc. London*, **286A**, 125–181, doi:10.1098/rsta.1977.0112.
- Trier, S. B., R. D. Sharman, R. G. Fovell, and R. G. Frehlich, 2010: Numerical simulation of radial cloud bands within the upper-level outflow of an observed mesoscale convective system. *J. Atmos. Sci.*, **67**, 2990–2999, doi:10.1175/2010JAS3531.1.
- Wilson, R., H. Luce, H. Hashiguchi, N. Nishi, and Y. Yabuki, 2014: Energetics of persistent turbulent layers underneath mid-level clouds estimated from concurrent radar and radiosonde data. *J. Atmos. Sol.-Terr. Phys.*, **118**, 78–89, doi:10.1016/j.jastp.2014.01.005.
- Woods, J. D., 1968: Wave-induced shear instability in the summer thermocline. *J. Fluid Mech.*, **32**, 791–800, doi:10.1017/S0022112068001035.